A&A 511, A2 (2010)
DOI: 10.1051/0004-6361/200913135

Astronomy & Astrophysics

Trigonometric parallaxes of 6.7 GHz methanol masers

K. L. J. Rygl[1,⋆], A. Brunthaler[1], M. J. Reid[2], K. M. Menten[1], H. J. van Langevelde[3,4], and Y. Xu[5]

[1] Max-Planck-Institut für Radioastronomie (MPIfR), Auf dem Hügel 69, 53121 Bonn, Germany
e-mail: [kazi;brunthal;kmenten]@mpifr-bonn.mpg.de
[2] Harvard-Smithsonian Center for Astrophysics, 60 Garden Street, Cambridge, MA 02138, USA
e-mail: reid@cfa.harvard.edu
[3] Joint Institute for VLBI in Europe, Postbus 2, 7990 AA Dwingeloo, The Netherlands
e-mail: langevelde@jive.nl
[4] Sterrewacht Leiden, Leiden University, Postbus 9513, 2300 RA Leiden, The Netherlands
[5] Purple Mountain Observatory, Chinese Academy of Sciences, Nanjing 21008, PR China
e-mail: xuye@pmo.ac.cn

Received 18 August 2009 / Accepted 30 September 2009

ABSTRACT

Aims. Emission from the 6.7 GHz methanol maser transition is very strong, is relatively stable, has small internal motions, and is observed toward numerous massive star-forming regions in the Galaxy. Our goal is to perform high-precision astrometry using this maser transition to obtain accurate distances to their host regions.
Methods. Eight strong masers were observed during five epochs of VLBI observations with the European VLBI Network between 2006 June, and 2008 March.
Results. We report trigonometric parallaxes for five star-forming regions, with accuracies as good as ∼22 μas. Distances to these sources are $2.57^{+0.34}_{-0.27}$ kpc for ON 1, $0.776^{+0.104}_{-0.083}$ kpc for L 1206, $0.929^{+0.034}_{-0.033}$ kpc for L 1287, $2.38^{+0.13}_{-0.12}$ kpc for NGC 281-W, and $1.59^{+0.07}_{-0.06}$ kpc for S 255. The distances and proper motions yield the full space motions of the star-forming regions hosting the masers, and we find that these regions lag circular rotation on average by ∼17 km s^{-1}, a value comparable to those found recently by similar studies.

Key words. techniques: interferometric – astrometry – masers – stars: formation – ISM: molecules – Galaxy: kinematics and dynamics

1. Introduction

Accurate distances and proper motions are crucial for studies of the structure and kinematics of the Milky Way. Since we are in the Galactic plane, it is not easy to determine the spiral structure of our Milky Way (Reid et al. 2009b). Massive star-forming regions trace the spiral arms and are objects well-suited to revealing the structure of the Milky Way.

Determining the fundamental physical properties of individual objects, such as size scales, masses, luminosities, and ages, also depends critically on distance. For example, the distance to the Orion Nebula, determined by a number of trigonometric parallax measurements using radio continuum emission from stars in its associated cluster (Menten et al. 2007; Sandstrom et al. 2007), water masers (Hirota et al. 2007), and SiO masers (Kim et al. 2008), turned out to be 10% less than previously assumed, resulting in 10% lower masses, 20% fainter luminosities, and 20–30% younger ages for the stars in the cluster.

The most fundamental and unbiased method of measuring distances is the trigonometric parallax, which depends only on geometry and is therefore free of any astrophysical assumptions. To achieve the sub-milliarcsecond astrometric accuracy at optical wavelengths requires space-borne observations. The first dedicated optical satellite for this purpose was ESA's Hipparcos (Perryman et al. 1995). With its accuracy of 0.8–2 mas, it was capable of measuring distances up to ∼200 pc – only a small fraction of the Milky Way. A new optical astrometry satellite GAIA, to be launched in 2012, will be two orders of magnitude more accurate and push the optical parallaxes to Galactic size scales (e.g., Lindegren 2009). Despite the high accuracy, GAIA will suffer from dust extinction in the Galactic plane, in particular in the spiral arms and toward the Galactic center. Here radio astronomy can provide an important complement to GAIA, because radio wavelengths do not suffer from dust extinction, and Very-Long-Baseline Interferometry (VLBI) phase-referencing techniques can provide accuracies better than 10 μas, allowing accurate distances with errors less than 10% out to 10 kpc (see for example Honma et al. 2007; Hachisuka et al. 2009; Reid et al. 2009a).

Strong and compact radio sources, such as molecular masers, are ideal targets for trigonometric parallax measurements. Masers are frequently found in (dusty) star formation regions (SFRs) and asymptotic giant branch stars. The most numerous interstellar masers are the 22 GHz water masers, followed in number by the 6.7 GHz methanol masers; to date several hundreds of these masers have been found across the Galaxy (e.g., Pestalozzi et al. 2005; Green et al. 2009). They are

⋆ Member of the International Max Planck Research School (IMPRS) for Astronomy and Astrophysics at the Universities of Bonn and Cologne.

Table 1. Observation information.

Program	Date	Participating antennas[a]
EB32A	10 Jun. 2006	Jb Wb Ef Mc Tr Nt Hh On Da
EB32B	18 Mar. 2007	Jb Wb Ef Mc Tr Nt Hh On Cm
EB32C	17 Jun. 2007	Jb Wb Ef Mc Tr Nt Hh On Cm
GB63A	31 Oct. 2007	Jb Wb Ef Mc Tr Nt Hh On Y1
GB63B	16 Mar. 2008	Jb Wb Ef Mc Tr Nt Hh On Y1

Notes. [(a)] The full names of the antennas are: Jb – Jodrell Bank; Wb – Westerbork (in single dish mode); Ef – Effelsberg; Mc – Medicina; Tr – Torun; Nt – Noto; Hh – Hartebeesthoek; On – Onsala; Da – Darnhall; Cm – Cambridge; Y1 – single EVLA antenna.

exclusively associated with early stages of massive star formation, observed both prior to the development of an ultra compact HII (UCHII) region and coexistent with these (Menten 1991; Ellingsen 2006; Pestalozzi et al. 2007). Maser modeling indicates that the 6.7 GHz emission is likely to be excited via radiative pumping by warm dust heated by newly formed high-mass stars (Sobolev et al. 2007).

Sources of methanol masers have long lifetimes of $\sim 10^4$ year (van der Walt 2005). Their velocity spread is typically within ± 5 km s^{-1} about the systematic velocity of the molecular core, and single maser features are usually narrow (~ 1 km s^{-1}). The kinematics suggest that methanol masers originate from different regions than water masers, which have wider velocity spreads and are produced in protostellar outflows (Menten 1996). To summarize, the strength, ubiquity, long lifetimes, and small internal motions make the 6.7 GHz methanol maser very suitable for astrometric purposes.

Here we present results from observations with the European VLBI Network (EVN) of eight strong methanol masers belonging to well-known massive SFRs in the outer part of the Milky Way: ON 1, L 1287, L 1206, NGC 281-W, MonR 2, S 252, S 255 and S 269. Recently, H_2O maser or 12.2 GHz methanol maser parallax measurements have been reported for three of these regions (NGC 281-W, Sato et al. 2008; S 252, Reid et al. 2009a; S 269, Honma et al. 2007), allowing a valuable cross check with our measurements. The results of this present work are crucial for star formation studies in these regions, and, together with a larger sample of parallaxes, will help to understand the structure of the Local and Perseus arms.

In this paper we report on the first parallax measurements made with the EVN. Results presented here replace preliminary, less accurate, and less complete measurements (Rygl et al. 2008). In the next section we describe the observations and data analysis, and in Sect. 3 we explain the method and fitting of the parallax and proper motion. The results are then presented per source in Sect. 4 and discussed in Sect. 5. The conclusions are summarized in Sect. 6.

2. Observations and data analysis

The observations were performed with the EVN at five epochs between 2006 June, and 2008 March. The exact dates of the observations and the participating antennas are listed in Table 1. Each observation lasted 24 h and made use of *geodetic-like* observations to calibrate the tropospheric zenith delays at each antenna (see Reid & Brunthaler 2004; Brunthaler et al. 2005; Reid et al. 2009a, for a detailed discussion). A typical observing run consisted of four 6-h blocks containing ~1 h of geodetic-like observations, ~10 min of observation of fringe finders. The remaining time was spent on maser/background source phase-referencing observations. During each run, the average on-source time per maser was between ~0.9 and ~1.2 h depending on the sky position, because half of our targets were low declination sources that had a limited visibility.

Using the technique of phase referencing, each maser was observed in a cycle with two (or one) nearby (~1°–2° separation) compact radio quasars, which were used as background sources. The sources were switched every 2 min. Before our EVN observations, we had used the NRAO Very Large Array under project AB1207 in A-configuration to observe several compact NVSS (Condon et al. 1998) sources within 1° from the maser source at two frequencies (8.4 and 4.8 GHz) to check their spectral index and compactness. For the best candidates, we determined their position to a sub-arcsecond accuracy to use them as a position reference in the EVN observations. Additionally, several known VLBA calibrators were used, namely: J2003+3034 and J0613+1708 (Fomalont et al. 2003), J0603+215S(9) and J0613+1306 (Ma et al. 1998), J0047+5657 (Beasley et al. 2002), J2223+6249 (Petrov et al. 2005), J0035+6130 (Petrov et al. 2006), and J0606-0724 (Kovalev et al. 2007). Table 2 lists the positions of the masers and their background sources.

The observations were performed with eight intermediate frequency bands (IF) of 8 MHz width, each in dual circular polarization sampled at the Nyquist rate with 2 bits per sample, yielding a recording rate of 512 Mbps. The data were correlated in two passes at the Joint Institute for VLBI in Europe (JIVE), using an integration time of 0.5 s, affording a field of view of 1.″2 (limited by time-averaging smearing). The maser data were correlated using one 8 MHz IF band with 1024 spectral channels, resulting in a channel separation of 7.81 kHz or 0.41 km s^{-1} at 6.7 GHz. The quasar sources were correlated in continuum mode with eight IFs of 8 MHz width with a channel separation of 0.25 MHz.

The data were reduced using the NRAO Astronomical Image Processing System (AIPS). The *geodetic-like* observations were reduced separately, and tropospheric delays were estimated for each antenna. The data were reduced following the EVN guidelines, applying parallactic angle and ionospheric delay corrections. The JIVE correlator model uses Earth's orientation parameters, which are interpolated from the appropriate daily-tabulated values, so it is not necessary to correct them after the correlation. The ionospheric delays were based on the JPL GPS–IONEX total vertical electron content maps of the atmosphere. Amplitudes were calibrated using system-temperature measurements and standard gain curves. A "manual phase-calibration" was performed to remove delay and phase differences between the IFs. The Earth rotation was corrected for with the task "CVEL". For each maser, a spectral channel with one bright and compact maser spot was used as the phase reference. The data was Hanning-smoothed to minmize Gibbs ringing in the spectral line data. To avoid the strong fluctuations caused by the band-pass edges, the outer two channels in each IF were discarded (following Reid et al. 2009a). The positions of the masers and background sources were extracted by fitting 2D Gaussians to the maps.

Here, we report the results on the first five sources for which we have completed the analysis: ON 1, L 1206, L 1287, NGC 281-W, and S 255. For the other sources, S 252, S 269, and MonR 2, we had problems with the calibration of the data, which were likely caused by residual atmospheric delay, so that we

Table 2. Source information.

Source	RA (J2000) (h:m:s)	Dec (J2000) (° : ′ : ″)	ϕ^a (°)	PA^a (°)	Brightness^b (Jy beam^{-1})	Restoring beam^b (mas, mas, deg)
ON 1	20:10:09.074	+31:31:35.946	...	...	1–7	5.7 × 3.9, 86
J2003+3034 ...	20:03:30.244	+30:34:30.789	1.71	–124	0.124	5.3 × 3.7, 76
J2009+3049 ...	20:09:17.588	+30:49:24.580	0.73	–14	0.008	5.6 × 3.7, 88
L 1206	22:28:51.407	+64:13:41.314	...	...	0.3–1.4	5.7 × 4.0,−80
J2223+6249 ...	22:23:18.097	+62:49:33.805	1.53	–157	0.093	5.7 × 3.9,−84
J2225+6411 ...	22:25:27.993	+64:11:15.030	0.37	–96	0.002	5.6 × 3.8,−80
L 1287	00:36:47.353	+63:29:02.162	...	...	0.5–4.1	6.0 × 4.1,−57
J0035+6130 ...	00:35:25.311	+61:30:30.761	1.98	–176	0.092	6.0 × 4.1,−58
J0037+6236 ...	00:37:04.332	+62:36:33.310	0.88	178	0.061	5.9 × 4.2,−57
NGC 281-W ...	00:52:24.196	+56:33:43.175	...	...	1–12	5.7 × 4.2,−56
J0047+5657 ...	00:47:00.429	+56:57:42.395	0.84	62	0.142	5.6 × 4.0,−65
J0052+5703 ...	00:52:54.303	+57:03:31.460	0.50	–8	0.010	5.6 × 3.9,−62
MonR 2	06:07:47.862	-06:22:56.518	...	...	9–22	8.6 × 4.4, 42
J0606-0724 ...	06:06:43.546	-07:24:30.232	1.06	–165	0.135	9.0 × 4.1, 40
S 252	06:08:53.344	+21:38:29.158	...	...	17-44	6.4 × 3.9, 56
J0603+215S ..	06:03:51.557	+21:59:37.698	1.22	–73	0.019	6.7 × 3.8, 54
S 255	06:12:54.020	+17:59:23.316	...	...	4	6.9 × 3.9, 56
J0613+1708 ...	06:13:36.360	+17:08:24.946	0.87	169	0.040	7.1 × 3.9, 46
S 269	06:14:37.055	+13:49:36.156	...	...	0.2–1.1	6.8 × 3.9, 58
J0613+1306 ...	06:13:57.693	+13:06:45.401	0.73	–167	0.087	6.8 × 3.8, 57

Notes. [(a)] Separation, ϕ, and the Position Angle (east of north), PA, between the maser and the background source; [(b)] the brightness and restoring beam (east of north) are listed for the second epoch.

were unable to achieve sufficient accuracy for a parallax measurement.

3. Method and fitting

The absolute positions of the masers were not known with milliarcsecond accuracy before our first observation. Only after the first epoch was analyzed were accurate positions determined. As a result, different correlator positions were used between the first and following epochs. In the first epoch, position errors above 0.″2 made it difficult to calibrate the phases because of a high fringe rate, which could not be interpolated correctly when applied to the data. Shifting the maser into the phase center turned out to be very time-consuming with available software because AIPS and the EVN correlator use apparent positions calculated at different times (AIPS at 0 UT of the first observing day versus the EVN correlator at the end of the first scan). Even an infinitesimally small shift in the epoch coordinate using the AIPS tasks "CLCOR" or "UVFIX" can result in a substantial position change and phase shifts from the old EVN apparent position to the new AIPS apparent position at 0 UT. In a parallax experiment, accurate and consistent positions throughout the experiment are crucial. Since it was difficult to calibrate the phases for masers with a large position offset or to shift these to the phase center, several sources in the first epoch could not be used for phase referencing. Although it should be possible to correct for this difference in registration, it would have required a software effort beyond the scope of the current project. Therefore we chose to discard some of the first-epoch data.

Most of the ionospheric delay is removed using measurements of the total electron content of the ionosphere obtained from dual-band global positioning system measurements (e.g., Ros et al. 2000). The expected residual delay is still a few centimeters, comparable to the residual tropospheric delay at the observing frequency. Our single frequency geodetic-like observations do not allow a separation of the ionospheric and tropospheric contributions. The measured group-delays from the geodetic blocks are interpreted as having a tropospheric origin, and the data are phase-delay-corrected accordingly. An ionospheric group delay makes a different contribution to the phase delay, so that the tropospheric correction can even deteriorate the calibration when the group delay has a partially ionospheric origin. Since the residual tropospheric delay is a few centimeters at 6 GHz and can easily be confused with an ionospheric residual, the tropospheric correction is not expected to be very useful in improving the quality of calibration. As a test, all data were reduced with and without a "tropospheric" delay correction. In slightly more than half of the cases, the signal-to-noise ratio improved by applying the tropospheric correction. We noted a trend toward improvement with decreasing declination: both high declination sources, $\delta \simeq 64°$, L 1206 and L 1287 improved in 2 out of 5 epochs; NGC 281-W at $\delta \simeq 57°$ improved in 3 out 5 epochs; and ON 1 at $\delta \simeq 31°$ even improved in 4 out of 5 epochs. Ionospheric delay saturates at zenith angles greater than ∼70°. However, the tropospheric delay continues to grow rapidly at larger zenith angles and can dominate the ionospheric delay at zenith angles of ∼80° (see Thompson et al. 1991).

For each SFR, we found the emission to arise from a number of separate maser spots. Most of the line profiles stretched over several channels. Both spatially and/or spectrally different maser spots were considered as distinct maser components. We inspected the behavior of the proper motion for each maser spot relative to the reference spot. Maser spots with strong nonlinear proper motions or a large scatter of position about a linear fit

were discarded. Only compact maser spots with well-behaved proper motions were used for the parallax fitting.

The average internal proper motion of the maser spots ranged between 0.06 and 0.23 mas yr^{-1}. Considering the distance of each maser, these proper motions correspond to 0.5–1 km s^{-1}, much lower than the internal proper motions of water masers, which can reach up to 20–200 km s^{-1} (Hachisuka et al. 2006). The only exception was ON 1, which separates into two distinct maser groups with a relative proper motion of 0.52 mas yr^{-1}, or 6.3 km s^{-1}. This particularity is discussed in Sect. 4.1.

The parallaxes and proper motions were determined from the change in the positions of the maser spot(s) relative to the background source(s). The data were fitted with a parallax and a linear proper motion. Since the formal position errors are only based on the signal-to-noise ratios determined from the images, they do not include possible systematic errors from residual zenith delay errors or source structure changes. This leads to a high reduced χ^2 value for the fits, so we added error floors in quadrature to the positions until reduced χ^2 values close to unity were reached for each coordinate.

First, we performed parallax and proper motion fits for each maser spot relative to one background source. Then we made combined fits with respect to each background source, assuming one parallax but different proper motions for each maser spot. Finally, we repeated this combined fit for both the background sources together. The position measurements of different maser spots are not independent, since systematic errors, such as an unmodeled atmospheric delay, will affect all maser spots in a similar way. If these systematic errors dominate, this will lead to unrealistically small errors. The most conservative approach, which we adopted, is to assume that the systematic errors are 100% correlated. Then the error of the combined fit has to be multiplied by $\sqrt{N}$, where N is the number of maser spots.

However, this will overestimate the error, if significant random errors are present (e.g., owing to maser blending and structural changes over time), since the latter are not correlated between different maser spots. Random errors can be reduced by averaging the positions of the different maser spots (following the approach of Bartkiewicz et al. 2008; Hachisuka et al. 2009). We calculated the average positions with respect to each background source after removing their position offsets and proper motions. Then, we performed a parallax fit on these averaged data sets relative to each individual background source, and on both the background sources combined. This approach has the advantage that we can reduce the random errors, while leaving the systematic errors intact. In Table 5 we list the individual parallax and proper motion fits to each maser spot, the combined fit of all the maser spots and the fit of the averaged data sets.

For most masers, we observed two background sources. Some of these background source pairs show a variation in their separation (mimicking a proper motion) of up to 1–2 mas yr^{-1} (on average this apparent movement was 0.54 mas yr^{-1}). This apparent movement is much greater than expected for extragalactic sources measured at 12 GHz, <0.1 mas yr^{-1} (Reid et al. 2009a) or 22 GHz, <0.02 mas yr^{-1} (Brunthaler et al. 2007). While at higher frequencies, the radio emission is typically dominated by the flat spectrum radio cores, the steep spectrum emission from the radio jets becomes stronger at lower frequencies. Thus, structure changes in these jets can lead to apparent motions, even if these jets are unresolved. At the distances of the respective masers, these apparent movements correspond to 2–10 km s^{-1}. Since we do not know which of the two background sources is responsible for this movement, the apparent movements of the background source pairs were added in quadrature to the final errors of the averaged proper motions of the masers. A summary of our parallaxes and proper motions is given in Table 3.

Table 3. Parallax and proper motion results.

Source	π (mas)	D_π (kpc)	$\mu_\alpha^{a,b}$ (mas yr^{-1})	μ_δ^{b} (mas yr^{-1})
ON 1	0.389 ± 0.045	$2.57^{+0.34}_{-0.27}$	-3.24 ± 0.89^{c}	-5.42 ± 0.46^{c}
L 1206	1.289 ± 0.153	$0.776^{+0.104}_{-0.083}$	0.27 ± 0.23	−1.40 ± 1.95
L 1287	1.077 ± 0.039	$0.929^{+0.034}_{-0.033}$	−0.86 ± 0.11	−2.29 ± 0.56
NGC 281-W	0.421 ± 0.022	$2.38^{+0.13}_{-0.12}$	−2.69 ± 0.16	−1.77 ± 0.11
S 255	0.628 ± 0.027	$1.59^{+0.07}_{-0.06}$	−0.14 ± 0.54	−0.84 ± 1.76

Notes. [a] The proper motion, μ_α, includes the factor $\cos(\delta)$; [b] the errors of the proper motion take the uncertainty resulting from an apparent nonzero movement between the background sources into account; [c] for the proper motion of ON 1, we took an average of the north and south components.

4. Individual sources

4.1. Onsala 1

The maser emission of Onsala 1 (ON 1) consists of two groups separated spatially by ~940 mas, which have different radial velocities by 15 km s^{-1} (Fig. 1). The northern group, which includes the reference channel, is centered at a $v_{\rm LSR}$ of ≈0 km s^{-1} and the southern group at ≈15 km s^{-1}. Four maser spots in the northern group were suitable for parallax fitting. The masers in the southern group were not used for the parallax fit, since the phase-calibration was less accurate because of the large distance to the phase-reference center (located in the northern maser group). We find a parallax of 0.389 ± 0.045 mas, corresponding to a distance of $2.57^{+0.34}_{-0.27}$ kpc. The proper motions of the southern maser spots were fitted by assuming the parallax result of the northern group. All results are listed in Table 5 and the parallax fit is plotted in Fig. 2.

For ON 1, two background sources were detected in epochs two through five (Fig. 3). The last (fifth) epoch had poor (u, v) coverage, which resulted in very elongated synthesized beams in the east-west direction (J2003+3034, 12.1 × 3.7 mas^2, PA ~ 87°; J2009+3049, 11.0 × 3.3 mas^2, PA ~ 88°) compared to the representative numbers listed in Table 2. As a result, the right ascension data had a large uncertainty in epoch five. We estimated this uncertainty from fitting the variation in the background-source pair separation to be 2 mas (see Fig. 4). Since this was a combined error for both the background sources, the position error for each individual background source was $\sqrt{2}$ mas. We added an additional error floor of $\sqrt{2}$ mas to the error given for all the right ascension data points in the fifth epoch. The apparent movements between the two background sources, J2003+3034–J2009+3049, were 0.88 ± 0.06 mas yr^{-1} in right ascension and 0.45 ± 0.21 mas yr^{-1} in declination (Fig. 4).

4.2. L 1206

In L 1206, two maser groups were found separated by ~100 mas. A third maser group was found northeast of the other two. This third maser group was not detected in all the epochs because of its weakness so was not used in the parallax measurements. Also

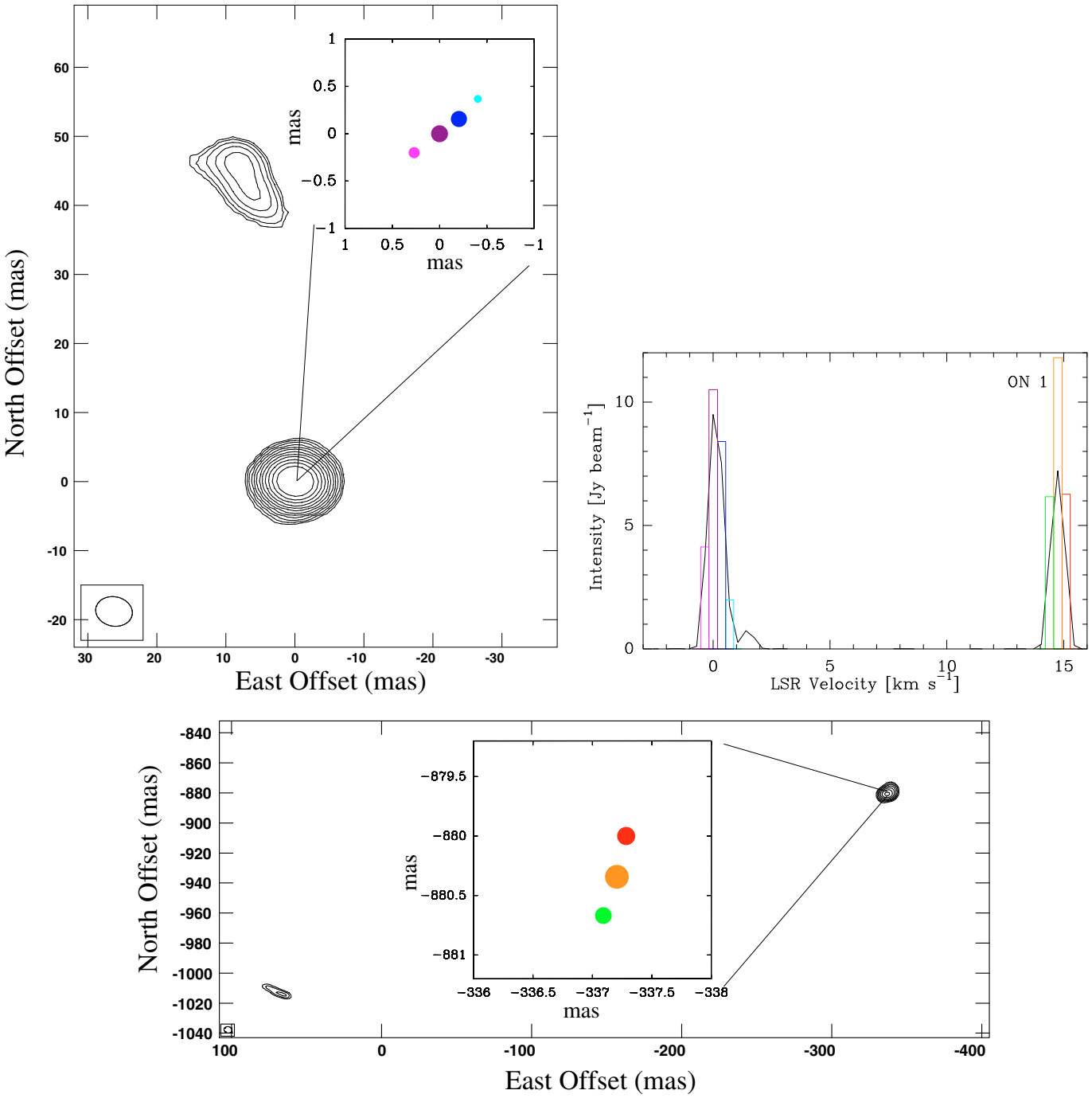

Fig. 1. Velocity-integrated maps of the northern (*top, left*) and southern (*bottom*) maser groups in ON 1, together with the spectrum (*top, right*). Position offset (0,0) corresponds to the position listed in Table 2. Maser spots are indicated with color codes for different radial velocities. The areas of the colored circles and the colored histogram entries in the spectrum are scaled to the peak flux of that spot. The black line in the spectrum is the intensity of the maser within a selected surface, which is not necessarily the same as the intensity of the maser spot retrieved from a Gaussian fit. For the northern group, the contour levels start at 0.1 Jy beam^{-1} km s^{-1}, in the southern group 1.0 Jy beam^{-1} km s^{-1}, and increase by factors of $\sqrt{2}$.

the maser spot at -11.6 km s^{-1} was omitted for the same reason. The masers in L 1206 are shown with a spectrum in Fig. 5. The parallax fit used four compact maser spots and resulted in 1.289± 0.153 mas, corresponding to a distance of $0.776^{+0.104}_{-0.083}$ kpc. The results of the parallax and proper motion fits are displayed in Fig. 6 and listed in Table 5.

Figure 7 shows the phase-referenced images for both background sources. Only one of the two background sources, J2225+6411, was detected in the first epoch. The other background source, J2223+6249, had a much larger separation from the maser (i.e., the phase reference) and the transfer of the phase solutions to the J2223+6249 data probably failed. The apparent movements between the background sources were 0.22 ± 1.45 mas yr^{-1} in right ascension and 1.91 ± 1.43 mas yr^{-1} in declination (Fig. 8).

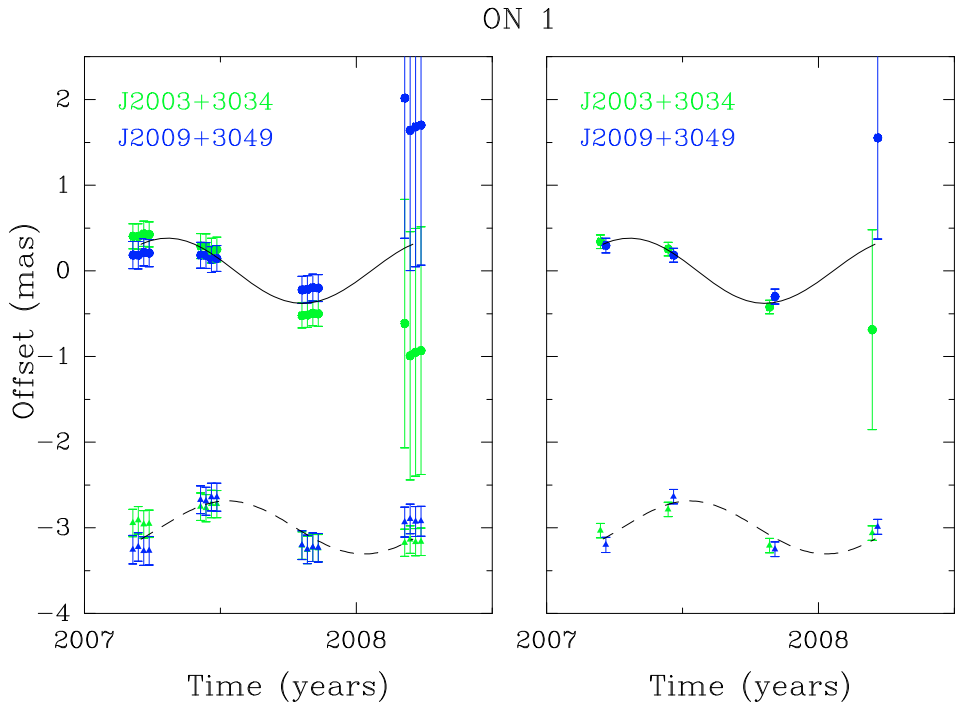

Fig. 2. Results of the parallax fit based on four maser spots. The *left graph* shows a combined fit on all data, the *right graph* is a fit on the averaged data sets. The filled colored dots mark the data points in right ascension, while the filled colored triangles mark the declination. The solid line is the resulting fit in right ascension, the dashed line in declination. Different colors indicate a different background source.

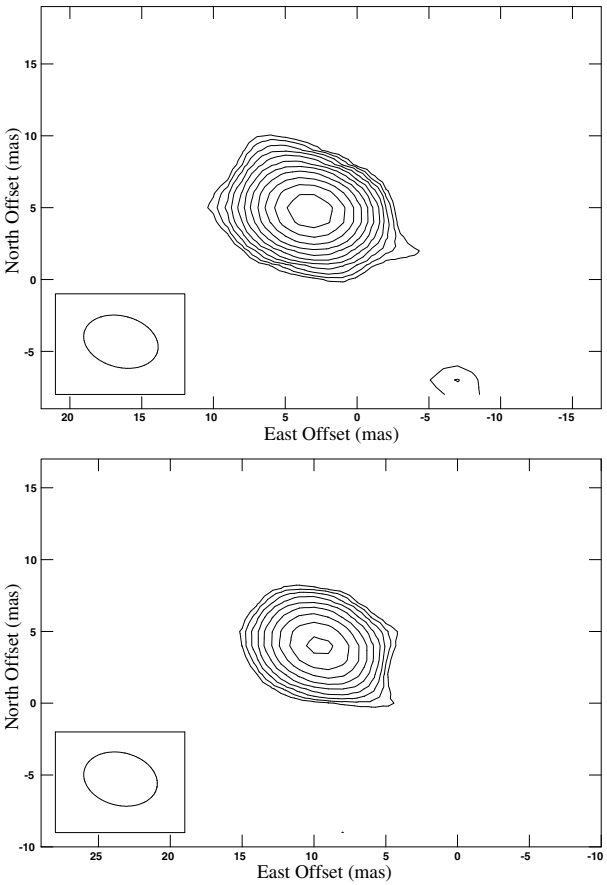

Fig. 3. Phase-referenced images for two background sources belonging to maser ON 1, J2003+3034 (*top*) and J2009+3049 (*bottom*) in the third epoch. Position offset (0, 0) corresponds to the position listed in Table 2. The contour levels start at a 3σ level, 6.1, and 0.6 mJy beam^{-1}, respectively, and increase by factors of $\sqrt{2}$.

4.3. L 1287

Toward L 1287 we find three maser groups, two close together (within ∼40 mas) and the third ∼135 mas southward, shown with a spectrum in Fig. 9. A total of six maser spots from the three groups were used for the parallax fit. We report a parallax value of 1.077 ± 0.039 mas, corresponding to a distance of $0.929^{+0.034}_{-0.033}$ kpc. The results are plotted in Fig. 10 and listed in Table 5.

Figure 11 shows the phase-referenced images for both background sources. The variation of the separation between the two background sources, J0035+6130 and J0037+6236, is shown in Fig. 12. Two data points appear to be outliers: the right ascension at epoch four and declination at epoch two. Increasing the data errors to 0.9 and 0.7 mas, respectively, for these outliers yields an apparent movement fit of −0.05 ± 0.12 mas yr^{-1} in right ascension and 0.54 ± 0.10 mas yr^{-1} in declination (Fig. 12). We investigated the visibility amplitudes as a function of (u, v) distance and found evidence of extended structure. For J0037+6236 at the fourth epoch, evidence of extended structure in the right ascension direction was found; however, for J0035+6130 at the second epoch, we found no indications of such structure.

4.4. NGC 281-W

We found four groups of methanol masers toward NGC 281-W, as illustrated in Fig. 13 together with the source spectrum. For the parallax fit we used a total of six maser spots coming from three groups, the central, southern, and southeast groups (Fig. 13). The weaker maser spots, like the ones located in the western group, were omitted in the parallax fitting. We find a parallax of 0.421 ± 0.022 mas corresponding to distance of $2.38^{+0.13}_{-0.12}$ kpc. The results are shown in Fig. 14 and listed in Table 5.

For NGC-281-W, two background sources were detected successfully at epochs two through five (Fig. 15). Background

Table 4. Peculiar motions.

Source	R_0 = 8.5 kpc, Θ_0 = 220 km s^{-1}			R_0 = 8.4 kpc, Θ_0 = 254 km s^{-1}		
	U (km s^{-1})	V (km s^{-1})	W (km s^{-1})	U (km s^{-1})	V (km s^{-1})	W (km s^{-1})
ON 1	18±8	−19±3	4±10	7±8	−21±3	4±10
L 1206	2±4	−16±2	0±6	−1±4	−16±2	0±6
L 1287	13±2	−18±2	−3±2	10±2	−18±2	−3±3
NGC 281-W	13±2	−3±2	−9±2	6±2	−3±2	−9±2
S 255	1±3	−4±12	3±7	2±3	−4±12	3±7

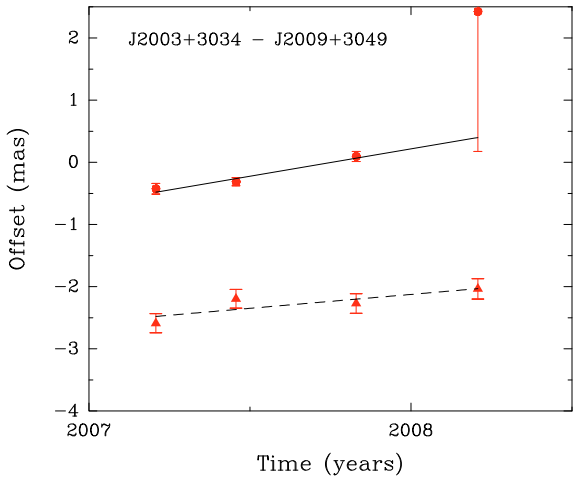

Fig. 4. Variation of the separation between background sources J2003+3034–J2009+3049 belonging to ON 1. The solid line and the dots represent the right ascension data, while the dashed line and the filled triangles represent the declination data.

source J0052+5703 showed a double structure with the weaker component located ∼25 mas westward of the stronger component (Fig. 15). The proper motion of the western component with respect to J0052+5703 was $\mu_\alpha = 0.64 \pm 0.63$ mas yr^{-1} and $\mu_\delta = -0.36 \pm 0.39$ mas yr^{-1} (Fig. 16), i.e., exhibiting no detectable proper motion. The apparent movement between the two background sources, J0047+5657 and J0052+5703, was also close to zero: -0.16 ± 0.13 mas yr^{-1} in right ascension and -0.11 ± 0.11 mas yr^{-1} in declination.

4.5. S 255

For S 255, we could only use emission from one maser channel, namely the reference channel. Based on this maser spot, at 4.6 km s^{-1} (Fig. 17), we find a parallax of 0.628 ± 0.027 mas corresponding to a distance of $1.59^{+0.07}_{-0.06}$ kpc. The results are shown in Fig. 18 and listed in Table 5.

We observed only one background source, J0613+1708, for S 255 (Fig. 19), which was detected in epochs two to five. With only one background source, we could not check that its apparent movement was small, and so, conservatively, we added uncertainties of 1 mas yr^{-1} in both coordinates.

5. Discussion

5.1. Space motions

With parallax and proper motion measurements, one can calculate the full space motion of the masers in an SFR in the Galaxy. Using an accurate model of Galactic dynamics (Galactic rotation

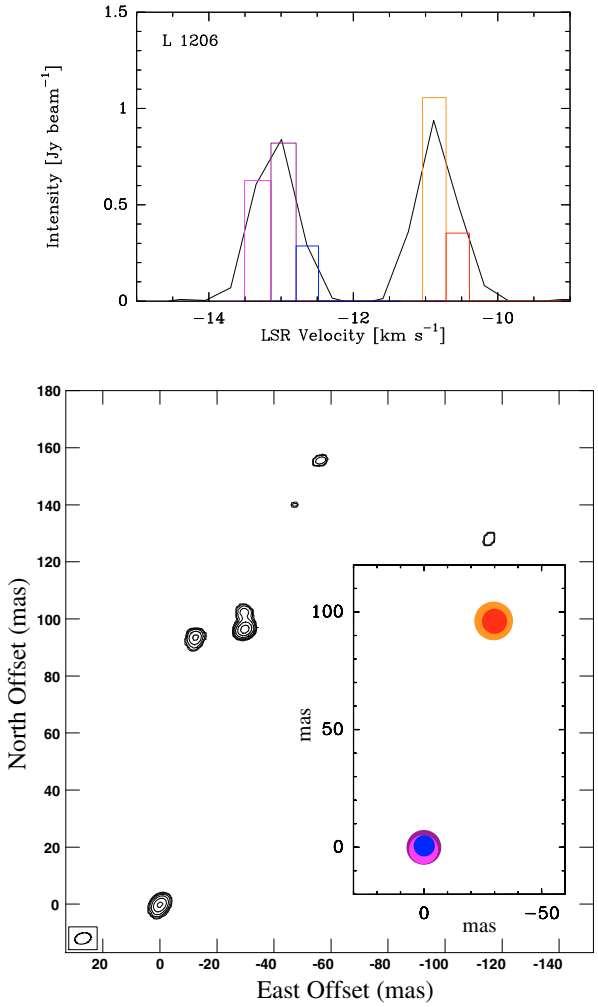

Fig. 5. Velocity-integrated map and spectrum of L 1206. Position offset (0,0) corresponds to the position listed in Table 2. Maser spots are indicated with color codes for different radial velocities. The areas of the colored circles and the colored histogram entries in the spectrum are scaled to the peak flux of that spot. The black line in the spectrum is the intensity of the maser within a selected surface, which is not necessarily the same as the intensity of the maser spot retrieved from a Gaussian fit. The diffuse and weak spots were omitted, such as the spot at (–10,95). Contour levels start at 0.1 Jy beam^{-1} km s^{-1} and increase by factors of $\sqrt{2}$.

speed, Θ_0, distance of the Sun to the Galactic center, R_0, rotation curve) for a source and removing the modeled contribution of Galactic rotation allows one to retrieve source peculiar motion relative to a circular orbit. The peculiar motion is described by the vectors U, V, and W, locally toward the Galactic center, toward the direction of rotation and toward the North Galactic Pole, respectively.

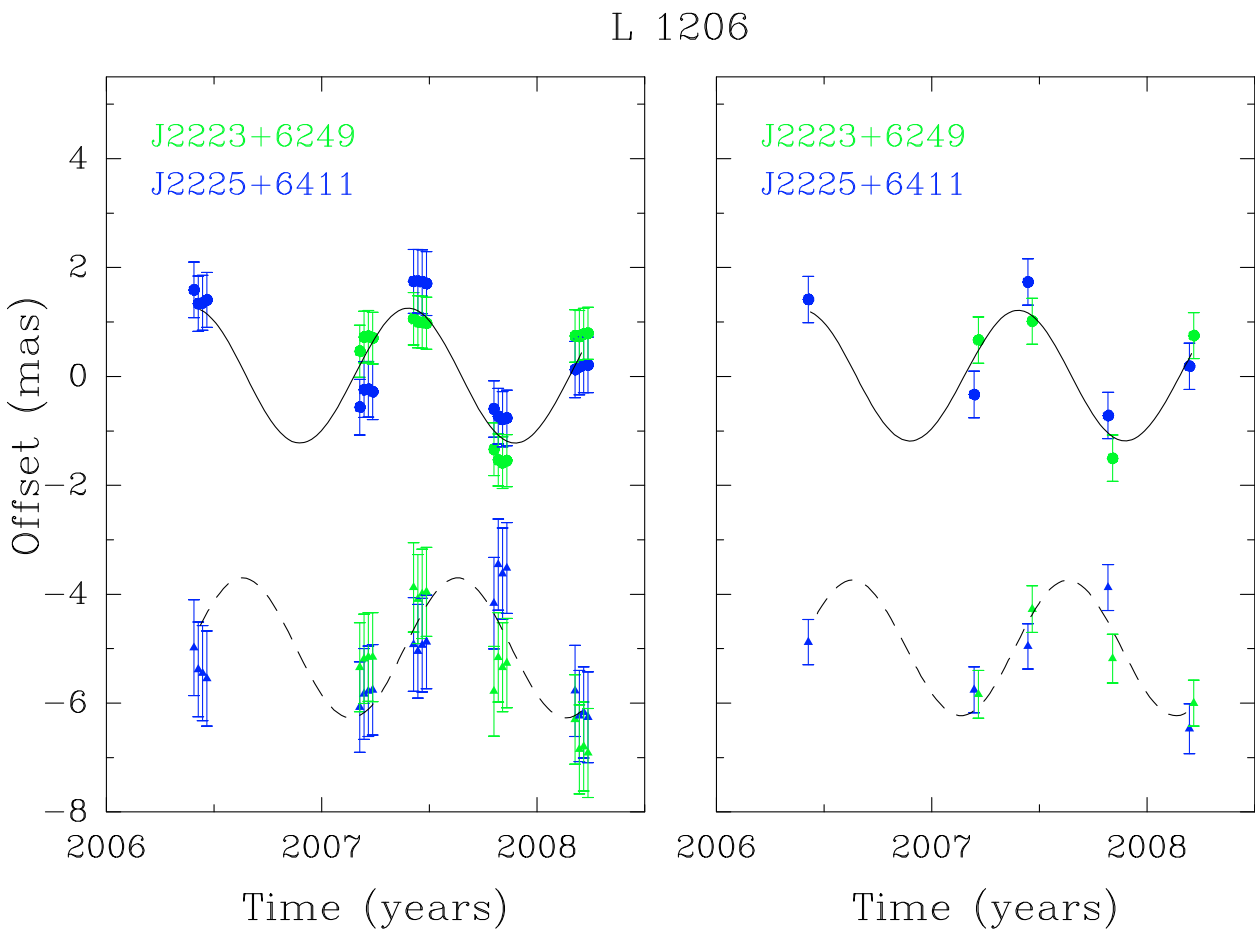

Fig. 6. Results of the parallax fit for L 1206 based on four maser spots. The *left graph* shows a combined fit on all data, the *right graph* is a fit on the averaged data sets. The filled dots mark the data points in right ascension, while the filled triangles mark the declination. The solid line is the resulting fit in right ascension, the dashed line in declination. Different colors indicate different background sources.

In Table 4, the peculiar motions of our sources are given for two different Galactic models: the IAU recommended values for the LSR motion $R_0 = 8.5$ kpc, $\Theta_0 = 220$ km s^{-1} in Cols. 2–4; a new model with $R_0 = 8.4$ kpc, $\Theta_0 = 254$ km s^{-1}, based on a large sample of trigonometric parallax measurements (Reid et al. 2009b), in Cols. 5–7. Both models adopt the Hipparcos values for the Solar motion (Dehnen & Binney 1998) and assume a flat rotation curve. We used the parallaxes and proper motions as are listed in Table 3, where the uncertainty introduced by the apparent movement of the background sources was included in the proper motion uncertainty of the source.

In Fig. 20 we plot the SFRs studied in this work at their determined distances with their peculiar motion in the Galactic plane, after removing the Galactic rotation. For either model, it is clear that three SFRs show a similar lag on circular rotation as the SFRs studied by Reid et al. (2009b), while two have a circular rotation close to zero lag. For NGC 281-W, the zero lag can be understood from its large distance from the Galactic disk ($b \simeq -6°$) and the dominant contribution from the expanding super bubble to the peculiar motion of this SFR (see Sect. 5.5). For S 255, it is not clear why its circular velocity is close to Galactic rotation (Sect. 5.6). The motion towards the Galactic center, U, tends to be positive for most of the SFRs.

Recently, McMillan & Binney (2009) have published a reanalysis of the maser astrometry presented by Reid et al. (2009b). They fitted the data with the revised solar peculiar motion of Binney (2009), mentioned in McMillan & Binney (2009), where the V component of the solar peculiar velocity, $V_\odot$, is increased from 5.2 km s^{-1} to 11 km s^{-1}. With a larger $V_\odot$ the lag of SFRs on Galactic rotation would decrease to ∼11 km s^{-1}, which agrees with the expected velocity dispersion for young stars of ∼10 km s^{-1} (Aumer & Binney 2009). However, even when considering the revised $V_\odot$, we note that most SFRs still rotate more slowly than the Galactic rotation (by ∼11 km s^{-1}) and that their velocities are not randomly dispersed.

5.2. Onsala 1

Our trigonometric parallax measurement places ON 1 on a distance from the Sun of $2.57^{+0.34}_{-0.27}$ kpc, somewhat closer than the (near) kinematic distance of 3.0 kpc, based on the methanol maser line at 15 km s^{-1}. The latter assumes a flat rotation curve with as distance of the Sun to the Galactic center, $R_0 = 8.5$ kpc, and for the Galactic rotation speed, $\Theta_0 = 220$ km s^{-1}. However, it is farther than the commonly adopted (near) kinematic distance of 1.8 kpc based on formaldehyde at $v_{\rm LSR} = 11.2$ km s^{-1} (MacLeod et al. 1998) using the Galactic rotation curve of Wouterloot & Brand (1989), with $R_0 = 8.5$ kpc, $\Theta_0 = 220$ km s^{-1}. Our result resolves the near/far kinematic distance ambiguity and locates ON 1 in the Local spur consistent with the near kinematic distance.

We found different proper motions for the northern and southern maser groups (Table 5). The resulting difference in the east-west direction was small, $\mu_\alpha = 0.18 \pm 0.24$ mas yr^{-1}, but in the north-south direction, the southern group was moving by $\mu_\delta = -0.77 \pm 0.12$ mas yr^{-1} away from the northern group. At

Table 5. Detailed results of parallax and proper motions measurements.

Background source	v_{LSR} (km s^{-1})	Parallax (mas)	μ_α (mas yr^{-1})	μ_δ (mas yr^{-1})
		ON 1		
		Northern group		
J2003+3034	–0.4	0.521 ± 0.055	−3.33 ± 0.18	−5.26 ± 0.41
	0.0	0.401 ± 0.052	−3.72 ± 0.17	−5.26 ± 0.21
	0.4	0.361 ± 0.052	−3.82 ± 0.17	−5.28 ± 0.19
	0.7	0.526 ± 0.057	−3.36 ± 0.19	−5.19 ± 0.34
	Combined fit	0.299 ± 0.112[1]		
	Averaging data	0.391 ± 0.061		
J2009+3049	–0.4	0.380 ± 0.121	−2.87 ± 0.39	−4.88 ± 0.31
	0.0	0.459 ± 0.140	−2.68 ± 0.46	−4.80 ± 0.22
	0.4	0.483 ± 0.142	−2.59 ± 0.48	−4.79 ± 0.20
	0.7	0.415 ± 0.112	−2.81 ± 0.37	−4.78 ± 0.23
	Combined fit	0.482 ± 0.137[1]		
	Averaging data	0.368 ± 0.070		
		Southern group		
J2003+3034	14.4		−3.88 ± 0.12	−5.92 ± 0.14
	14.8		−3.75 ± 0.09	−6.03 ± 0.11
	15.1		−3.67 ± 0.21	−6.09 ± 0.19
J2009+3034	14.4		−3.00 ± 0.15	−5.49 ± 0.20
	14.8		−2.88 ± 0.21	−5.59 ± 0.26
	15.1		−2.77 ± 0.29	−5.65 ± 0.35
Both QSOs	Combined fit	0.390 ± 0.116[1]		
	Averaging data	**0.389 ± 0.045**		
$\langle\mu\rangle_{\rm north}(\sigma)_{pm}$			−3.15 ± 0.89(0.44)[2]	−5.03 ± 0.46(0.22)[2]
$\langle\mu\rangle_{\rm south}(\sigma)_{pm}$			−3.33 ± 0.90(0.45)[2]	−5.80 ± 0.46(0.23)[2]
		L 1206		
J2223+6249	–13.3	1.163 ± 0.222	0.24 ± 0.85	−2.84 ± 0.40
	–12.9	1.116 ± 0.263	0.08 ± 0.92	−2.59 ± 0.48
	–10.9	1.083 ± 0.170	0.23 ± 0.90	−2.85 ± 0.23
	–10.5	1.485 ± 0.190	0.56 ± 0.31	−1.61 ± 1.42
	Combined fit	1.318 ± 0.282[1]		
	Averaging data	1.331 ± 0.180		
J2225+6411	–13.3	1.311 ± 0.408	0.22 ± 0.51	−0.28 ± 0.63
	–12.9	1.322 ± 0.386	0.41 ± 0.50	−0.65 ± 0.56
	–10.9	1.300 ± 0.416	0.35 ± 0.52	−0.50 ± 0.65
	–10.5	1.174 ± 0.237	0.05 ± 0.64	0.11 ± 0.27
	Combined fit	1.272 ± 0.384[1]		
	Averaging data	1.288 ± 0.241		
Both QSOs	Combined fit	1.331 ± 0.250[1]		
	Averaging data	**1.289 ± 0.153**		
$\langle\mu\rangle(\sigma)_{pm}$			0.27 ± 0.23(0.16)[2]	−1.40 ± 1.95(1.15)[2]
		L 1287		
J0035+6130	–27.0	1.111 ± 0.074	−0.18 ± 0.10	−2.30 ± 0.25
	–23.9	0.928 ± 0.078	−1.02 ± 0.12	−2.28 ± 0.08
	–23.5	0.957 ± 0.093	−0.93 ± 0.11	−2.48 ± 0.12
	–23.2	1.002 ± 0.084	−0.88 ± 0.11	−2.39 ± 0.09
	–22.8	0.940 ± 0.083	−1.14 ± 0.11	−2.78 ± 0.10
	–22.5	0.917 ± 0.067	−1.17 ± 0.12	−3.28 ± 0.07
	Combined fit	0.984 ± 0.086[1]		
	Averaging data	1.016 ± 0.052		
J0037+6236	–27.0	1.306 ± 0.071	−0.14 ± 0.10	−1.71 ± 0.40
	–23.9	1.244 ± 0.044	−0.88 ± 0.04	−1.72 ± 0.27
	–23.5	1.225 ± 0.040	−0.81 ± 0.04	−1.77 ± 0.25
	–23.2	1.011 ± 0.101	−0.88 ± 0.14	−1.83 ± 0.12
	–22.8	0.945 ± 0.125	−1.17 ± 0.20	−2.20 ± 0.14

Table 5. continued.

Background source	v_{LSR} (km s^{-1})	Parallax (mas)	μ_α (mas yr^{-1})	μ_δ (mas yr^{-1})
	–22.5	1.330 ± 0.043	−1.01 ± 0.04	−2.64 ± 0.37
	Combined fit	1.192 ± 0.107[1]		
	Averaging data	1.150 ± 0.052		
Both QSOs	Combined fit	1.079 ± 0.069[1]		
	Averaging data	**1.077 ± 0.039**		
$\langle\mu\rangle(\sigma)_{pm}$			−0.86 ± 0.11(0.33)[2]	−2.29 ± 0.56(0.46)[2]
		NGC 281-W		
J0047+5657	–30.2	0.416 ± 0.054	−2.64 ± 0.15	−1.75 ± 0.10
	–29.9	0.380 ± 0.045	−2.54 ± 0.12	−1.72 ± 0.08
	–29.5	0.401 ± 0.041	−2.58 ± 0.19	−1.72 ± 0.07
	–29.2	0.404 ± 0.047	−2.69 ± 0.22	−1.75 ± 0.08
	–28.8	0.497 ± 0.026	−2.55 ± 0.04	−1.69 ± 0.13
	–28.1	0.529 ± 0.028	−2.68 ± 0.04	−1.52 ± 0.14
	Combined fit	0.400 ± 0.070[1]		
	Averaging data	0.398 ± 0.042		
J0052+5703	–30.2	0.459 ± 0.049	−2.79 ± 0.06	−1.87 ± 0.27
	–29.9	0.420 ± 0.048	−2.68 ± 0.05	−1.84 ± 0.25
	–29.5	0.388 ± 0.048	−2.75 ± 0.05	−1.84 ± 0.22
	–29.2	0.408 ± 0.054	−2.87 ± 0.07	−1.87 ± 0.20
	–28.8	0.602 ± 0.056	−2.65 ± 0.07	−1.82 ± 0.26
	–28.1	0.648 ± 0.055	−2.76 ± 0.07	−1.65 ± 0.34
	Combined fit	0.399 ± 0.054[1]		
	Averaging data	0.425 ± 0.024		
Both QSOs	Combined fit	0.412 ± 0.045[1]		
	Averaging data	**0.421 ± 0.022**		
$\langle\mu\rangle(\sigma)_{pm}$			−2.69 ± 0.16(0.10)[2]	−1.77 ± 0.11(0.10)[2]
		S 255		
J0613+1708	4.6	**0.628 ± 0.027**	−0.14 ± 0.05	−0.84 ± 1.67
μ_{pm}			−0.14 ± 0.54[2]	−0.84 ± 1.76[2]

Notes. [(1)] The error of the combined fit multiplied by $\sqrt{N}$, where N is the number of maser spots; [(2)] we calculated an unweighted arithmetic mean of the individual proper motion results from all maser spots and background sources. The error bar on the mean is the standard error of the mean to which was added, in quadrature, the apparent movement between the two background sources of the respective coordinate. The uncertainty in the proper motion, which is introduced by the background source, is hereby taken into account. In parenthesis is given the standard deviation of the mean.

a distance of 2.6 kpc, this corresponds to a relative speed of 9.4 km s^{-1}.

This large proper motion may be explained by the masers being located in the molecular gas surrounding an expanding HII region, as suggested by Fish & Reid (2007) and Su et al. (2009). The HII region is located at (α = 20^{h}10^{m}09^s.03, δ = +31°31′35″.4, J2000) and between the two maser groups. The radial velocity of the HII region, from the H76α recombination line, is 5.1±2.5 km s^{-1} (Zheng et al. 1985). The methanol masers would be (with respect to the rest frame of ON 1 at 5.1 km s^{-1}) in a blue-shifted component at ∼0 km s^{-1}, northward, and a red-shifted component at ∼15 km s^{-1}, southward of the HII region. Also, the hydroxyl masers in ON 1 provide some confirmation of this scenario (Nammahachak et al. 2006; Fish & Reid 2007). The expansion velocities of the masers, calculated by assuming a linear expansion from the center of the HII region, would be 5.8 km s^{-1} and 3.6 km s^{-1} for the northern and southern maser groups, respectively.

5.3. L 1206

For L 1206, the trigonometric parallax distance, $0.776^{+0.104}_{-0.083}$ kpc, is shorter than the kinematic distance; 1.0 kpc (based on a hydroxyl maser, at v_{LSR} = −8.5 km s^{-1}, using the Galactic rotation curve of Wouterloot & Brand (1989) with R_0 = 8.5 kpc, Θ_0 = 220 km s^{-1}, MacLeod et al. 1998), 1.23 kpc (ammonia, v_{LSR} = −9.9 km s^{-1}, using the Galactic rotation curve of Brand & Blitz (1993), with R_0 = 8.5 kpc, Θ_0 = 220 km s^{-1} Molinari et al. 1996) and 1.4 kpc (6.7 GHz methanol, flat rotation curve, R_0 = 8.5 kpc, Θ_0 = 220 km s^{-1}). Our result places L 1206 in the Local spur. Cep A, a nearby (3°.8 separation, PA 126°) star-forming region, is located at a distance of 700 ± 39 pc, as determined by a parallax measurement of 12.2 GHz methanol masers (Moscadelli et al. 2009). The L 1206 SFR therefore seems to be in the same part of the Local arm as Cep A. L 1206 is a dark cloud with an infrared source, IRAS 22272+6358A, which coincides with the methanol maser emission and a 2.7 mm dust continuum peak (Beltrán et al. 2006). Since neither 2 cm nor 6 cm radio emission is detected (Wilking et al. 1989; McCutcheon et al. 1991), L 1206 is thought to be in a young phase prior to the formation of an HII region. Beltrán et al. (2006) report large CO outflows, and put the systemic velocity of the ambient medium between [−13.5, −8.5] km s^{-1}, consistent with our systemic velocity range of [−13.3, −10.9] km s^{-1}.

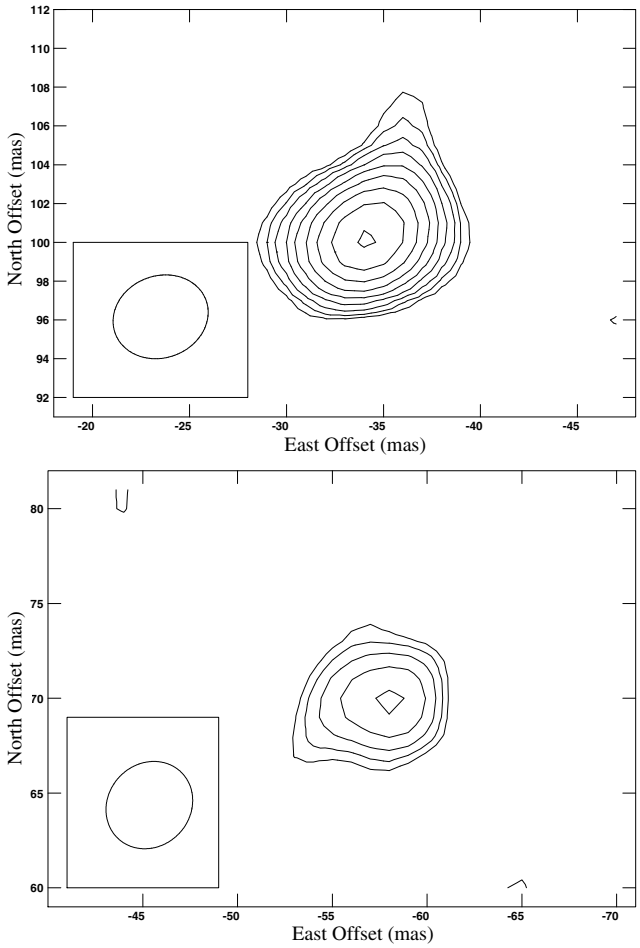

Fig. 7. Phase-referenced images for two background sources belonging to maser L 1206, J2223+6249 (*top*) and J2225+6411 (*bottom*) in the fifth epoch. Position offset (0,0) corresponds to the position listed in Table 2. Contour levels start at a 3σ level, 3.5, and 0.5 mJy beam^{-1} respectively, and increase by factors of $\sqrt{2}$.

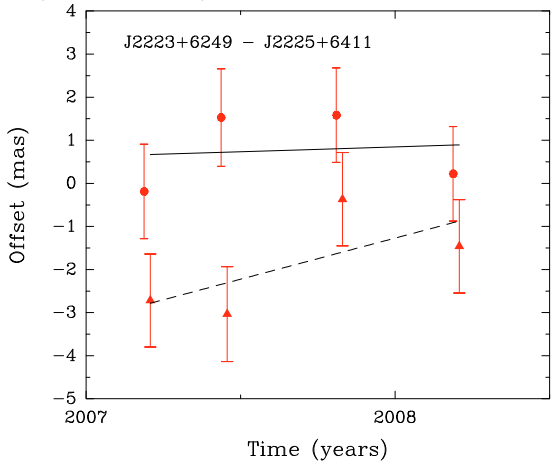

Fig. 8. Variation of the separation between background sources J2223+6249–J2225+6411 belonging to L 1206. The solid line and the dots represent the right ascension data, while the dashed line and the filled triangles represent the declination data.

5.4. L 1287

The parallax for L 1287 sets it at a distance of $0.929^{+0.034}_{-0.033}$ kpc. This is close to the photometric distance of ~850 pc from (Yang et al. 1991), which placed L 1287 in the Local arm. However, the kinematic distance based on the methanol maser line would place L 1287 at 2 kpc in the Perseus arm.

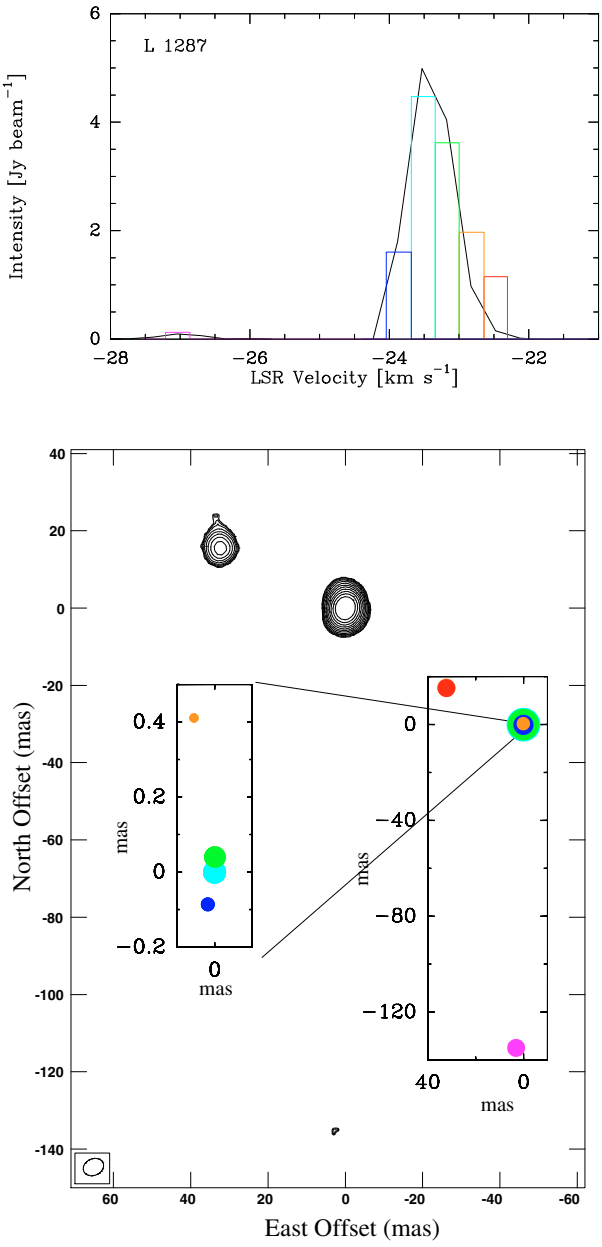

Fig. 9. Velocity-integrated map and spectrum of L 1287. Position offset (0,0) corresponds to the position listed in Table 2. Maser spots are indicated with color codes for different radial velocities. The areas of the colored circles and the colored histogram entries in the spectrum are scaled to the peak flux of that spot. The black line in the spectrum is the intensity of the maser within a selected surface, which is not necessarily the same as the intensity of the maser spot retrieved from a Gaussian fit. Contour levels start at 0.05 Jy beam^{-1} km s^{-1} and increase by factors of $\sqrt{2}$.

Methanol masers in the dark cloud L 1287 are located at the base of the bipolar CO outflow (Yang et al. 1991) originating in the main core of the cloud. The infrared point source (IRAS 00338+6312) in the center of the core indicates a protostellar object surrounded by cold, high density NH_3 (1, 1) gas (Estalella et al. 1993).

5.5. NGC 281-W

There are numerous distance estimates for NGC 281-W in the literature. Optical photometry places the cloud between 2 and

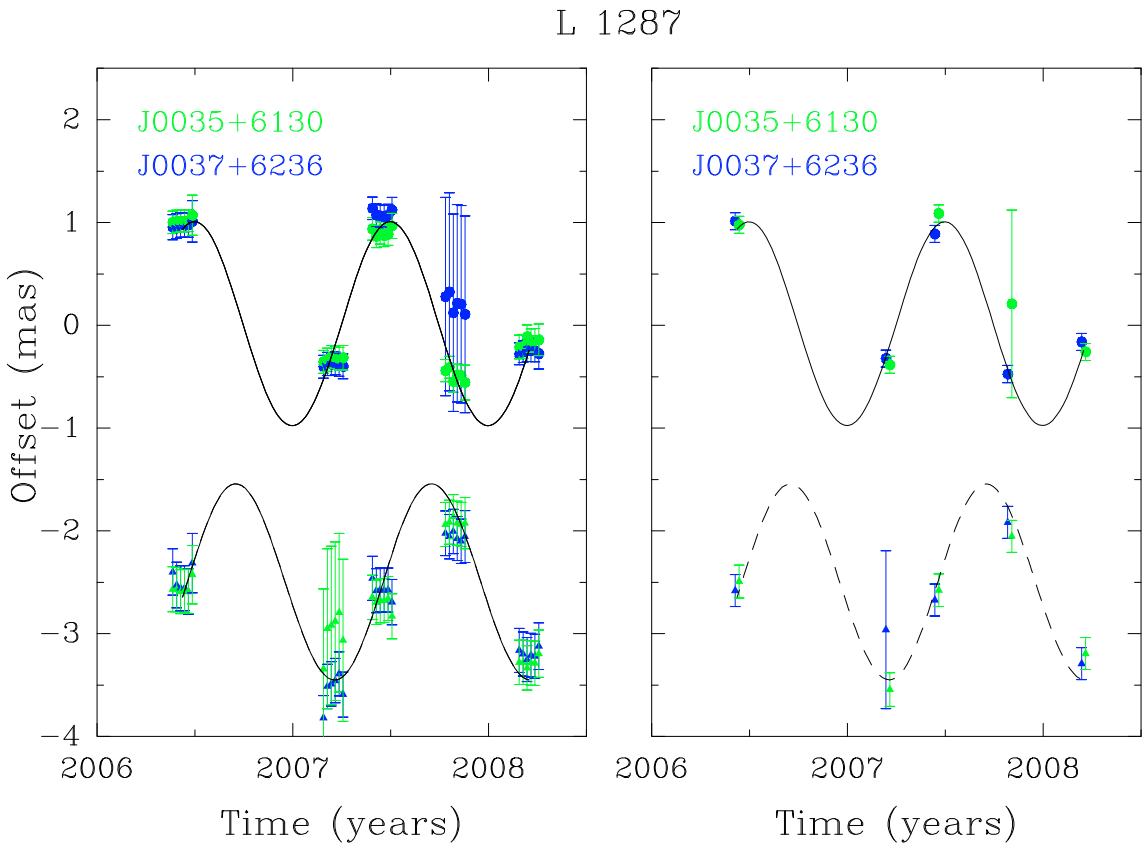

Fig. 10. Results of the parallax fit for L1278 based on six maser spots. The *left graph* shows a combined fit on all data, while the *right graph* is a fit on the averaged data sets. The filled dots mark the data points in right ascension, while the filled triangles mark the declination. The solid line is the resulting fit in right ascension, the dashed line in declination. Different colors indicate a different background source.

3.68 kpc (Sharpless 1954; Cruz-González et al. 1974; Henning et al. 1994; Guetter & Turner 1997), while the kinematic distance is 3 kpc (Lee & Jung 2003), based on a $v_{\rm LSR} = -30\,{\rm km\,s^{-1}}$, using the Galactic rotation curve of Clemens (1985) and $R_0 = 8.5\,{\rm kpc}, \theta_0 = 220\,{\rm km\,s^{-1}}$. The radial velocity of the methanol maser line at $-29\,{\rm km\,s^{-1}}$, assuming a flat Galactic rotation curve, and $R_0 = 8.5$ kpc, $\theta_0 = 220\,{\rm km\,s^{-1}}$, would place NGC 281-W at 2.5 kpc.

Recently, Sato et al. (2008) reported a water maser parallax value of 0.355 ± 0.030 mas, measured with the VERA interferometer, corresponding to a distance of 2.82 ± 0.24 kpc. We measured a parallax of 0.421 ± 0.022 mas, arriving at a distance of $2.38^{+0.13}_{-0.12}$ kpc. These distance measurements agree with Sato et al. (2008) within 2σ of the joint uncertainty. Also, our proper motion agrees within 1σ with the proper motion by Sato et al. (2008), and our radial velocity ($v_{\rm LSR} \sim -29\,{\rm km\,s^{-1}}$) is close to that of the water masers ($v_{\rm LSR} \sim -31\,{\rm km\,s^{-1}}$). It is unlikely that the water and methanol masers originate at such different depths into the SFR that it would affect the distance. For example, in the SFR W3(OH), the water and methanol maser parallaxes are in good agreement (Xu et al. 2006; Hachisuka et al. 2006).

NGC 281-W is an SFR that lies near the edge of a super bubble in the Perseus arm (Megeath et al. 2003; Sato et al. 2007). Our slightly shorter distance would change the position of NGC 281-W on this super bubble. Another SFR located on this bubble has a parallax determined distance: IRAS 00420+5530 at 2.17 ± 0.05 kpc (Moellenbrock et al. 2009). This allows to compare the distances and peculiar motions of both SFRs, and check whether the expanding super bubble, with the expansion center at 2.5 kpc adopted after Sato et al. (2008), can be responsible for the peculiar motions of both of them. We calculated the peculiar motions of IRAS 0042+5530 after Moellenbrock et al. (2009) and NGC 281-W after Sato et al. (2008) and our results. The bottom panel of Fig. 21 shows the peculiar motions in a face-on view of the Galactic plane. From the figure can be seen that the U component of NGC 281-W, representing the vector toward the Galactic center, is positive and non-zero in both our study and the work of Sato et al. (2008). This means that NGC 281-W is moving toward the Galactic center, which is the expected movement for the near side of an expanding bubble. In the top panel of Fig. 21 the peculiar motions of both SFRs are shown projected on a cross-section of the Galactic plane along the longitude of NGC 281-W, $l = 123°$. The average distance to NGC 281-W based on Sato et al. (2008) and this work, $2.58^{+0.27}_{-0.23}$ kpc, is marked in this panel as a cross. If we prolong the peculiar motion backwards of both IRAS 00420+5530 and the average result for NGC 281-W, they intersect at a distance from the Sun of 2.65 kpc and at a Galactic latitude of $\sim -0.^{\circ}1$. This suggets that, if indeed both SFRs are expanding linearly from one expansion center, the expansion center is offset from the previously assumed position. However, this offset center of expansion is difficult to understand when looking at the peculiar motion of both SFRs in the Galactic plane (Fig. 21, bottom panel), since the motion does not seem to originate in one mutual expansion center; hence, it is difficult to pinpoint the characteristics of the super bubble if the peculiar motions and distances of only two SFRs are all that are known.

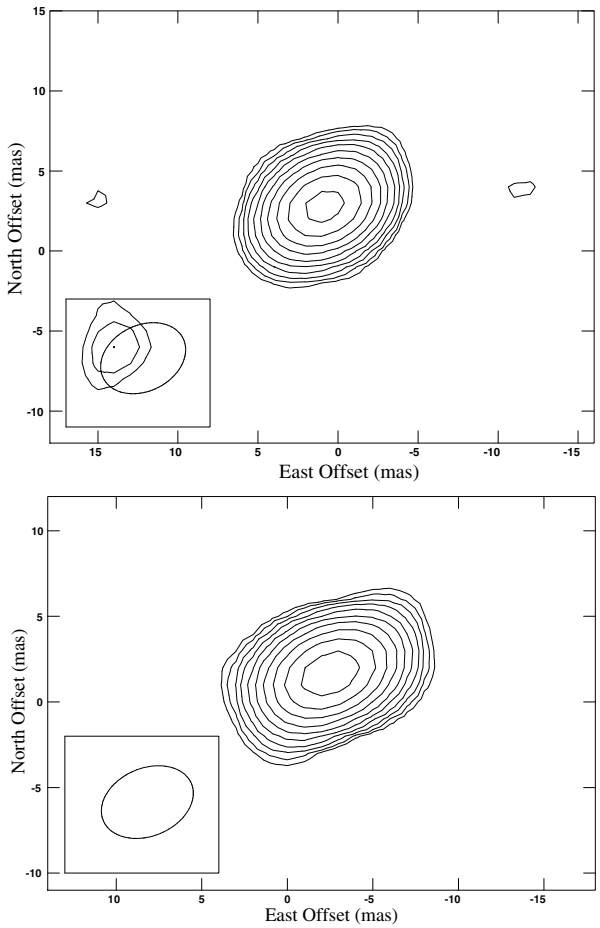

Fig. 11. Phase-referenced images for two background sources belonging to maser L 1287, J0035+6130 (*top*) and J0037+6236 (*bottom*) in epoch three. Position offset (0,0) corresponds to the position listed in Table 2. Contour levels start at a 3σ level, 3.6, and 2.4 mJy beam^{-1} respectively, and increase by factors of $\sqrt{2}$.

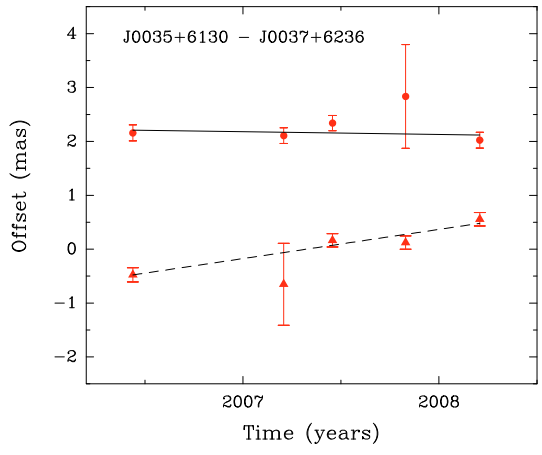

Fig. 12. Variation of the separation between background sources J0035+6130–J0037+6236 belonging to L 1287. The solid line and the dots represent the right ascension data, while the dashed line and the filled triangles represent the declination data.

5.6. S 255

For S 255, the parallax distance, $1.59^{+0.07}_{-0.06}$ kpc, is much closer than the commonly used photometric distance of 2.5 kpc (Moffat et al. 1979; Blitz et al. 1982). S 255 is an individual HII region, associated with a complex of HII regions. The methanol maser emission coincides with a filament of cold dust and molecular gas between two HII regions, S 255 and S 257. Minier et al. (2007) studied the star formation in this filament, which they propose is possibly triggered by the compression of the filament by the two HII regions. They find several molecular clumps in this filament. At distance of ≈2.5 kpc, the masses of the clumps, determined from the submillimeter dust continuum, are around 300 $M_\odot$ (Minier et al. 2007). However, if we place S 255 at the parallax determined distance of 1.6 kpc, the clump masses would drop by 60% to ∼120 $M_\odot$.

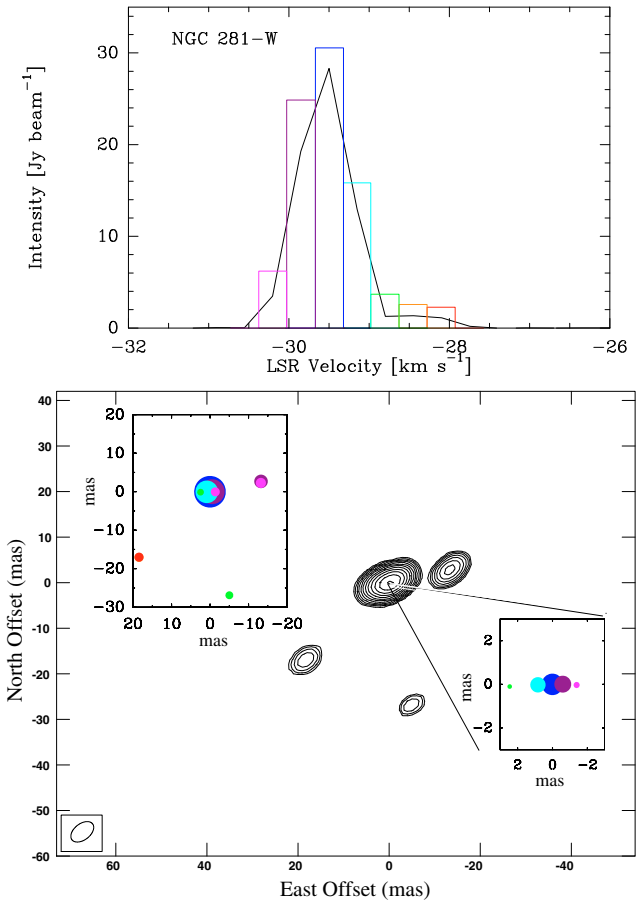

Fig. 13. Velocity-integrated map and spectrum of NGC 281-W. Position offset (0,0) corresponds to the position listed in Table 2. Maser spots are indicated with color codes for different radial velocities. The areas of the colored circles and the colored histogram entries in the spectrum are scaled to the peak flux of that spot. The black line in the spectrum is the intensity of the maser within a selected surface, which is not necessarily the same as the intensity of the maser spot retrieved from a Gaussian fit. Contour levels start at 0.5 Jy beam^{-1} km s^{-1} and increase by factors of $\sqrt{2}$.

6. Summary

We measured parallaxes of 6.7 GHz methanol masers using the EVN towards five SFRs, achieving accuracies approaching 20 μas. The primary results are summarized as follows:

1. We report trigonometric parallaxes for five star-forming regions, the distances to these sources are $2.57^{+0.34}_{-0.27}$ kpc for ON 1, $0.776^{+0.104}_{-0.083}$ kpc for L 1206, $0.929^{+0.034}_{-0.033}$ kpc for L 1287, $2.38^{+0.13}_{-0.12}$ kpc for NGC 281-W, and $1.59^{+0.07}_{-0.06}$ kpc for S 255.
2. Galactic star-forming regions lag circular rotation on average by ∼17 km s^{-1}, a value comparable to those found recently by similar studies (Reid et al. 2009b).

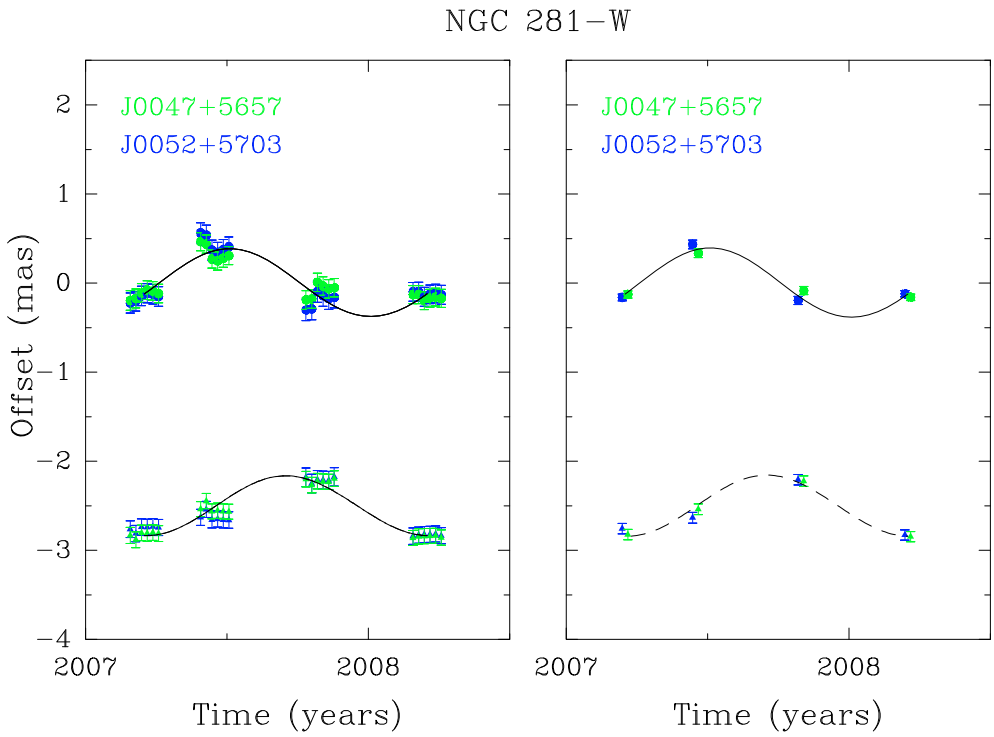

Fig. 14. Results of the parallax fit for NGC 281-W based on six maser spots. The *left graph* shows a fit on all data, while the *right graph* is a fit on the averaged data sets. The filled dots mark the data points in right ascension, while the filled triangles mark the declination. The solid line is the resulting fit in right ascension, the dashed line in declination. Different colors indicate a different background source.

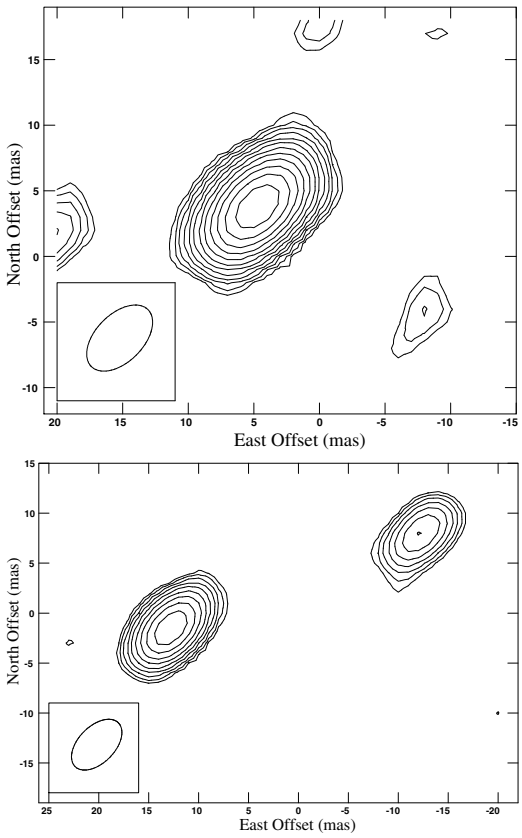

Fig. 15. Phase-referenced images for two background sources belonging to maser NGC 281-W, J0047+5657 (*top*) and J0052+5703 (*bottom*) in epoch five. Position offset (0,0) corresponds to the position listed in Table 2. Contour levels start at a 3σ level, 2.8, and 0.6 mJy beam^{-1} respectively, and increase by factors of $\sqrt{2}$. The bottom image shows also the additional component ~25 mas westward of J0052+5703.

3. Individual 6.7 GHz methanol maser spots are stable over a period of >2 years for most of the maser spots. The internal motions of the maser spots are weak (~0.5−1 km s^{-1}) and rectilinear.
4. Measurements at 6.7 GHz are less disturbed by the troposphere, as expected. However, the ionospheric delay cannot be ignored and is likely not to be completely removed by using the JPL GPS–IONEX maps to calculate propagation delays. Continuum measurements of background sources show that most of them have significant structure that is evident from the large (up to 1–2 mas, or 2–10 km s^{-1}) apparent movements between pairs of background sources. This additional uncertainty from the apparent movement does not prohibit a determination of the peculiar motion; however, it increases the error bars of the peculiar motion by the order of the uncertainty, depending on the distance and longitude of the source. The parallax uncertainty can be affected as well, if the cause of the apparent movement between the background sources are internal structure changes, which do not need to be perfectly linear. Two background sources should be a minimum for astrometric measurements at 6.7 GHz, so three or more background sources are recommended.

Acknowledgements. The European VLBI Network is a joint facility of European, Chinese, South African, and other radio astronomy institutes funded by their national research councils. The National Radio Astronomy Observatory is a facility of the National Science Foundation operated under cooperative agreement by Associated Universities, Inc. We thank the staff at JIVE, especially Bob Campbell, for technical help and support. We thank Amy Mioduszewski (NRAO) for her help with VLA frequency setup. K.L.J.R. was supported for this research through a stipend from the International Max Planck Research School (IMPRS) for Astronomy and Astrophysics at the Universities of Bonn and Cologne. Y.X. was supported by Chinese NSF through grants NSF 10673024, 10703010, and 10621303.

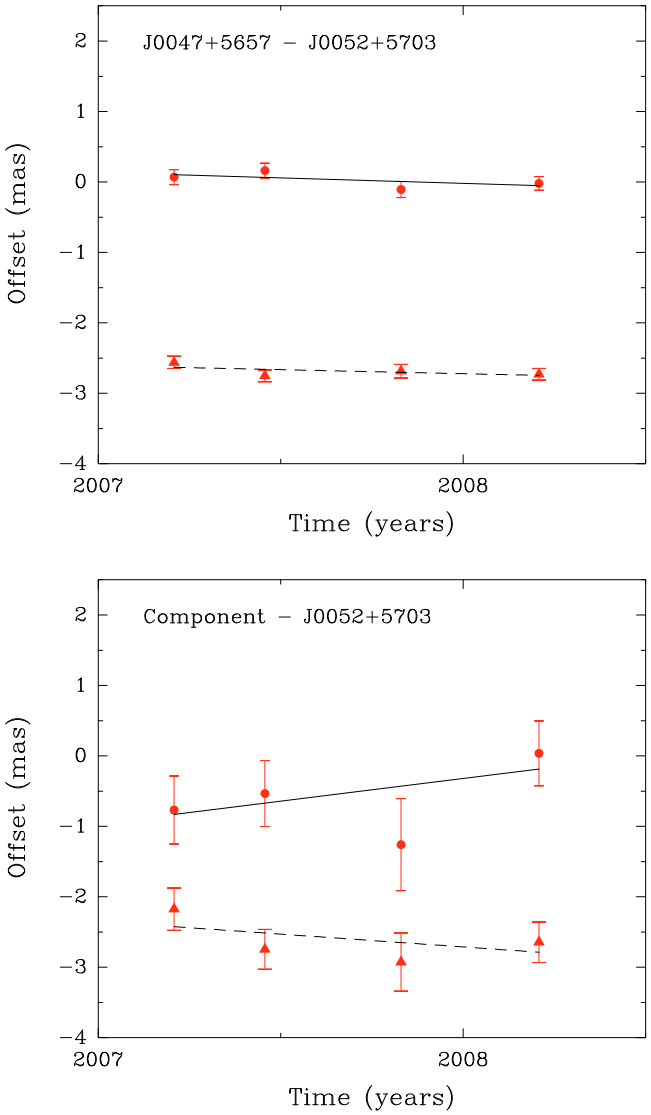

Fig. 16. *Left*: variation of the separation between background sources J0047+5657–J0052+5703 belonging to NGC 281-W. *Right*: the proper motion fit on the component of J0052+5703 with respect to the central source J0052+5703. The solid line and the dots represent the right ascension data, while the dashed line and the filled triangles represent the declination data.

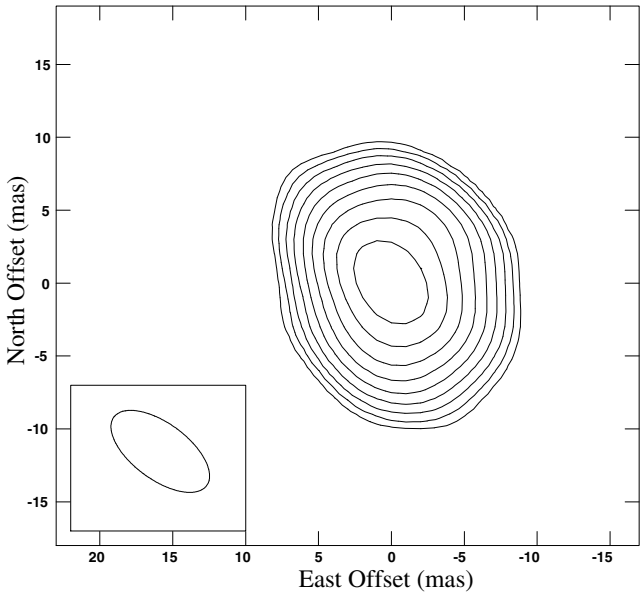

Fig. 17. Phase-referenced image for maser S 255 at channel 4.6 km s^{-1}. Position offset (0,0) corresponds to the position listed in Table 2. Contour levels start at 0.23 Jy beam^{-1}, and increase by factors of $\sqrt{2}$.

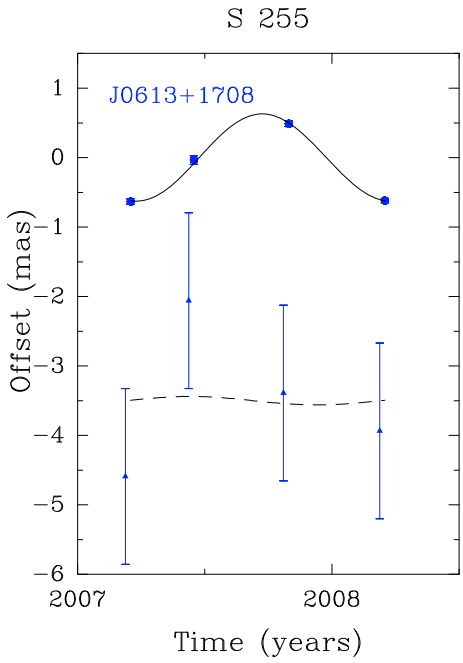

Fig. 18. Results of the parallax fit for S 255 based on one maser spot at 4.6 km s^{-1}. The filled dots mark the data points in right ascension, while the filled triangles mark the declination. The solid line is the resulting fit in right ascension, the dashed line in declination.

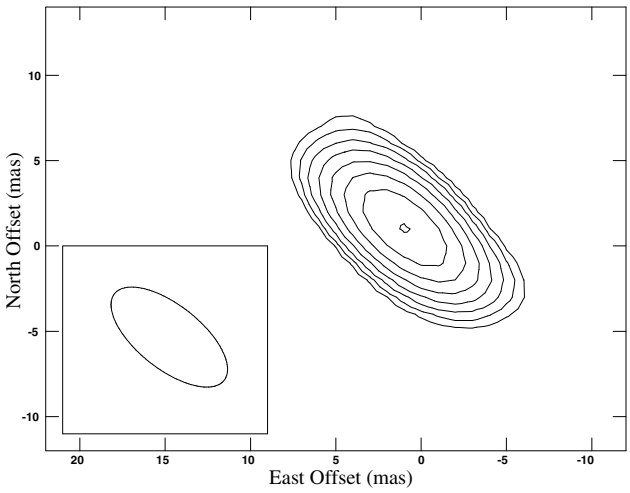

Fig. 19. Phase-referenced images for background source J0613+1708 belonging to maser S 255, in the third epoch. Position offset (0,0) corresponds to the position listed in Table 2. The contour levels start at a 3σ level, 3.0 mJy beam^{-1}, and increase by factors of $\sqrt{2}$.

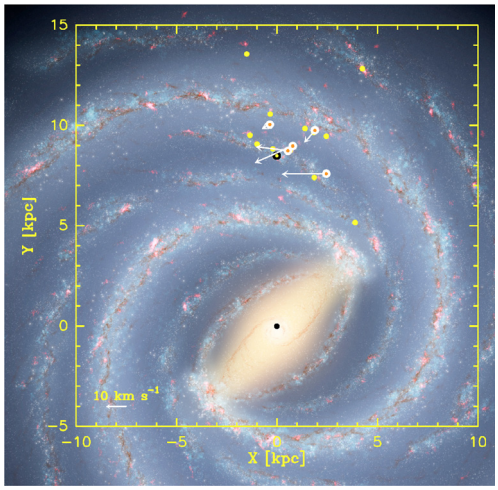

Fig. 20. An artist's impression of a plane-on view of our Galaxy (image credit: R. Hurt NASA/JPL-Caltech/SSC), overlaid with parallax measurements of water and methanol masers between $60° < l < 240°$ taken from Reid et al. (2009b), in which recent parallax measurements have been put together to study the Galactic structure. The black dot marks the Galactic center, the yellow dot encircled with black the Sun, the yellow dots mark the parallaxes taken from the literature, the orange dots encircled with white, and white arrows mark the parallaxes and peculiar motions obtained in this work. The peculiar motions are shown after removing the Galactic rotation assuming the values of $R_0 = 8.4$ kpc and $\Theta_0 = 254$ km s^{-1}.

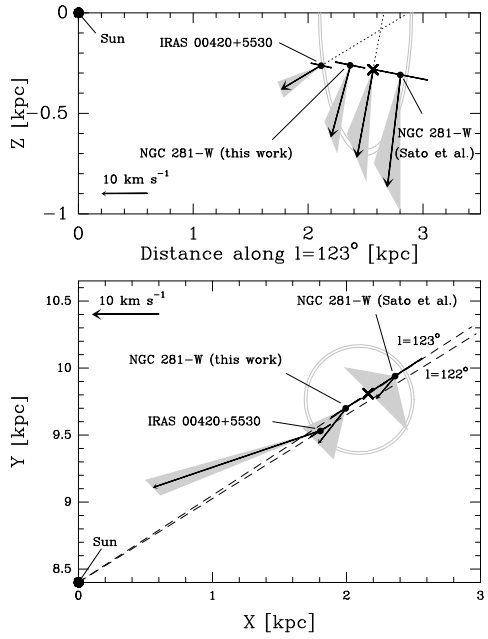

Fig. 21. *Lower panel*: a face-on view of the Galactic plane. The Galactic longitudes of NGC 281-W ($l \simeq 123°$) and IRAS 00425530 ($l \simeq 122°$) are indicated by dashed lines. The *top panel* shows a cross-section of the Galactic plane along the Galactic longitude of NGC 281-W (123°). The vertical coordinate of this plot is the direction perpendicular to the Galactic plane. We plot NGC 281-W and IRAS 00420+5530 as black dots, together with the respective distance error. Black arrows show the peculiar motion of the source after removing the Galactic rotation ($R_0 = 8.4$ kpc, $\Theta_0 = 254$ km s^{-1}). The errors in peculiar motion are indicated by the gray cones. The light-gray circles mark the super bubble with the center of the bubble at a distance of 2.5 kpc and a radius of 0.4 kpc, adopted after Sato et al. (2008). The cross marks the averaged distance of 2.58 kpc. The dotted lines show the backward prolongation of the proper motion of NGC 281-W and IRAS 00420+5530.

References

Aumer, M., & Binney, J. J. 2009, MNRAS, 896
Bartkiewicz, A., Brunthaler, A., Szymczak, M., van Langevelde, H. J., & Reid, M. J. 2008, A&A, 490, 787
Beasley, A. J., Gordon, D., Peck, A. B., et al. 2002, ApJS, 141, 13
Beltrán, M. T., Girart, J. M., & Estalella, R. 2006, A&A, 457, 865
Blitz, L., Fich, M., & Stark, A. A. 1982, ApJS, 49, 183
Brand, J., & Blitz, L. 1993, A&A, 275, 67
Brunthaler, A., Reid, M. J., & Falcke, H. 2005, in Future Directions in High Resolution Astronomy, ed. J. Romney, & M. Reid, ASP Conf. Ser., 340, 455
Brunthaler, A., Reid, M. J., Falcke, H., Henkel, C., & Menten, K. M. 2007, A&A, 462, 101
Clemens, D. P. 1985, ApJ, 295, 422
Condon, J. J., Cotton, W. D., Greisen, E. W., et al. 1998, AJ, 115, 1693
Cruz-González, C., Recillas-Cruz, E., Costero, R., Peimbert, M., & Torres-Peimbert, S. 1974, Rev. Mex. Astron. Astrof., 1, 211
Dehnen, W., & Binney, J. J. 1998, MNRAS, 298, 387
Ellingsen, S. P. 2006, ApJ, 638, 241
Estalella, R., Mauersberger, R., Torrelles, J. M., et al. 1993, ApJ, 419, 698
Fish, V. L., & Reid, M. J. 2007, ApJ, 670, 1159
Fomalont, E. B., Petrov, L., MacMillan, D. S., Gordon, D., & Ma, C. 2003, AJ, 126, 2562
Green, J. A., Caswell, J. L., Fuller, G. A., et al. 2009, MNRAS, 392, 783
Guetter, H. H., & Turner, D. G. 1997, AJ, 113, 2116
Hachisuka, K., Brunthaler, A., Menten, K. M., et al. 2006, ApJ, 645, 337
Hachisuka, K., Brunthaler, A., Menten, K. M., et al. 2009, ApJ, 696, 1981
Henning, T., Martin, K., Reimann, H.-G., et al. 1994, A&A, 288, 282
Hirota, T., Bushimata, T., Choi, Y. K., et al. 2007, PASJ, 59, 897
Honma, M., Bushimata, T., Choi, Y. K., et al. 2007, PASJ, 59, 889

Kim, M. K., Hirota, T., Honma, M., et al. 2008, PASJ, 60, 991
Kovalev, Y. Y., Petrov, L., Fomalont, E. B., et al. 2007, AJ, 133, 1236
Lee, Y., & Jung, J.-H. 2003, New Astron., 8, 191
Lindegren, L. 2009, Relativity in Fundamental Astronomy: Dynamics, Reference Frames, and Data Analysis 27 April–1 May, Virginia Beach, VA, USA, #16.01; BAAS, 41, 890, Amer. Astron. Soc., #261. 1601
Ma, C., Arias, E. F., Eubanks, T. M., et al. 1998, AJ, 116, 516
MacLeod, G. C., Scalise, E. J., Saedt, S., Galt, J. A., & Gaylard, M. J. 1998, AJ, 116, 1897
McCutcheon, W. H., Sato, T., Dewdney, P. E., et al. 1991, AJ, 101, 1435
McMillan, P. J., & Binney, J. J. 2009, MNRAS, submitted [arXiv:0907.4685]
Megeath, S. T., Biller, B., Dame, T. M., et al. 2003, in Winds, Bubbles, and Explosions: a conference to honor John Dyson, ed. J. Arthur, & W. J. Henney, Rev. Mex. Astron. Astrofis. Conf. Ser., 15, 151
Menten, K. M. 1991, ApJ, 380, L75
Menten, K. M. 1996, in Molecules in Astrophysics: Probes & Processes, ed. E. F. van Dishoeck, IAU Symp., 178, 163
Menten, K. M., Reid, M. J., Forbrich, J., et al. 2007, A&A, 474, 515
Minier, V., Peretto, N., Longmore, S. N., et al. 2007, in IAU Symp., ed. B. G. Elmegreen, & J. Palous, 237, 160
Moellenbrock, G. A., Claussen, M. J., & Goss, W. M. 2009, ApJ, 694, 192
Moffat, A. F. J., Jackson, P. D., & Fitzgerald, M. P. 1979, A&AS, 38, 197
Molinari, S., Brand, J., Cesaroni, R., et al. 1996, A&A, 308, 573
Moscadelli, L., Reid, M. J., Menten, K. M., et al. 2009, ApJ, 693, 406
Nammahachak, S., Asanok, K., Hutawarakorn Kramer, B., et al. 2006, MNRAS, 371, 619
Perryman, M. A. C., Lindegren, L., Kovalevsky, J., et al. 1995, A&A, 304, 69
Pestalozzi, M. R., Minier, V., & Booth, R. S. 2005, A&A, 432, 737
Pestalozzi, M. R., Chrysostomou, A., Collett, J. L., et al. 2007, A&A, 463, 1009
Petrov, L., Kovalev, Y. Y., Fomalont, E., et al. 2005, AJ, 129, 1163
Petrov, L., Kovalev, Y. Y., Fomalont, E. B., et al. 2006, AJ, 131, 1872
Reid, M. J., & Brunthaler, A. 2004, ApJ, 616, 872
Reid, M. J., Menten, K. M., Brunthaler, A., et al. 2009a, ApJ, 693, 397
Reid, M. J., Menten, K. M., Zheng, X. W., et al. 2009b, ApJ, 700, 137
Ros, E., Marcaide, J. M., Guirado, J. C., Sardón, E., & Shapiro, I. I. 2000, A&A, 356, 357
Rygl, K. L. J., Brunthaler, A., Menten, K. M., Reid, M. J., & van Langevelde, H. J. 2008, in Proceedings of the 9th European VLBI Network Symposium, on The role of VLBI in the Golden Age for Radio Astronomy and EVN Users Meeting. September 23–26, Bologna, Italy. Online at http://pos.sissa.it/cgi-bin/reader/conf.cgi?confid=72, 58
Sandstrom, K. M., Peek, J. E. G., Bower, G. C., Bolatto, A. D., & Plambeck, R. L. 2007, ApJ, 667, 1161
Sato, M., Hirota, T., Honma, M., et al. 2007, PASJ, 59, 743
Sato, M., Hirota, T., Honma, M., et al. 2008, PASJ, 60, 975
Sharpless, S. 1954, ApJ, 119, 334
Sobolev, A. M., Cragg, D. M., Ellingsen, S. P., et al. 2007, in IAU Symp. 242, ed. J. M. Chapman & W. A. Baan, 81
Su, Y.-N., Liu, S.-Y., & Lim, J. 2009, ApJ, 698, 1981
Thompson, A. R., Moran, J. M., & Swenson, G. W. 1991, Interferometry and synthesis in radio astronomy, ed. A. R. Thompson, J. M. Moran, & G. W. Swenson
van der Walt, J. 2005, MNRAS, 360, 153
Wilking, B. A., Blackwell, J. H., Mundy, L. G., et al. 1989, ApJ, 345, 257
Wouterloot, J. G. A., & Brand, J. 1989, A&AS, 80, 149
Xu, Y., Reid, M. J., Zheng, X. W., et al. 2006, Science, 311, 54
Yang, J., Umemoto, T., Iwata, T., et al. 1991, ApJ, 373, 137
Zheng, X. W., Ho, P. T. P., Reid, M. J., et al. 1985, ApJ, 293, 522